



Enhancing the Thermoelectric Performance of Cu₂S/CuO Nanocomposites Through Energy-Filtering effect and Phonon Scattering

J. Mani¹ · S. Radha¹ · F. Jeni Prita¹ · R. Rajkumar¹ · M. Arivanandhan² · G. Anbalagan¹

Received: 22 August 2023 / Accepted: 19 September 2023 / Published online: 5 November 2023
© The Author(s), under exclusive licence to Springer Science+Business Media, LLC, part of Springer Nature 2023

Abstract

Recently, thermoelectric (TE) materials have seized great attention for their role in clean energy conversion applications. Cu₂S are p-type super-ionic conductors featuring a narrow band gap of 1.7 eV while exhibiting outstanding thermoelectric characteristics. The Cu₂S matrix and the CuO nanoinclusions were successfully synthesized via solvothermal and hydrothermal routes, respectively. The morphological observations made through scanning and transmission electron microscope ensured the homogeneous distribution of CuO nanoinclusions in the Cu₂S matrix, hence, the formation of standard Cu₂S/CuO composites. In this work, we have introduced a “combined strategy” to boost the figure of merit (zT). The Seebeck coefficient reached the maximum of 271.86 μVK⁻¹ at 573 K for the 20 wt% CuO sample (a 71.45% gain when compared to the pure Cu₂S) owing to the filtration of low-energy carriers at the CuO potential barriers (2.5 eV). The Cu₂S/20 wt% CuO sample achieved the minimum thermal conductivity values. At 573 K, We recorded a vast power factor value of 952.66 μWm⁻¹ K⁻² (32.23% gain) for the Cu₂S/15 wt% CuO sample. These values are vastly higher than previously reported for the copper sulfides-based TE materials. Consequently, an optimised zT value of 0.44 (214.29% gain) was accomplished for the Cu₂S/15 wt% CuO sample at 573 K. The strategy presented in our study can also be extended to other TE materials, especially for the promising copper chalcogenides to improve their zT values.

Keywords Cu₂S/CuO · Nanocomposite · Energy filtering · Phonon scattering · Enhanced power factor · Figure of merit (zT)

1 Introduction

The sharp rise in the worldwide energy consumption rate and demand for oils, growing concerns over the release of greenhouse gases, and climate change compel us to shift towards clean and sustainable forms of energy [1, 2]. Thermoelectric (TE) materials have gained a considerable fascination with their proficiency to directly transform waste heat into electric power without moving parts or working fluids. They are quiet, reliable, and pollution-free [3, 4]. The operating concept behind this is the Seebeck effect

(thermoelectric power generation) and the Peltier effect (thermoelectric cooling power refrigeration) [5, 6]. Commercial and efficient TE materials like Bi₂Te₃ [7], PbTe [8], BiSbTe [9], PbSe [10], and Cu₂Se [11] often use toxic and expensive elements. Thus, there is an intense search for earth-abundant, low-cost, less toxic, high-performance TE materials to meet global energy requirements.

Copper chalcogenides (Cu_xY, Y = S, Se, Te) are promising thermoelectric materials [12, 13]. The low electronegative difference between Cu and chalcogens results in a covalent nature and narrower band gap (s and p orbitals of chalcogens strongly mix with outer s and p orbitals of Cu) than copper oxides [14, 15]. Their forbearance for a long-range and high antisite defect concentration helps in achieving distinctive and profoundly tuneable heat and charge transport and optoelectronic and plasmonic properties [14]. A further intriguing feature of Cu chalcogenides is the fact that, as the temperature rises, the Cu ions become extremely mobile and try to orient themselves statistically on disparate

✉ G. Anbalagan
anbu24663@yahoo.co.in

¹ Department of Nuclear Physics, Guindy Campus, University of Madras, Chennai, Tamil Nadu, India

² Centre for Nanoscience and Technology, Anna University, Chennai, Tamil Nadu, India

locations, leading to a more ordered crystallographic symmetry depending on the chalcogen framework. Thus, at higher temperatures, they shift towards a further congruent phase, enhancing carrier transport properties [16–18].

The competence of TE devices exceedingly relies on a dimensionless term referred to as the figure of merit, given by.

$$zT = \frac{S^2\sigma}{k} T \quad (1)$$

where S , σ , κ and T denote the Seebeck coefficient, electrical conductivity, thermal conductivity, and absolute temperature, respectively. As S , σ and κ are strongly interrelated with each other, the independent optimisation of these variable to enhance the zT value, becomes a challenging task. In addition to that, the optimisation also depends on several factors like the crystal structure, phase, dopant amount, type, composition, and so on. Literature has disclosed that methods like designing complex crystal structures, superlattices, nanostructures, doping, alloying, band gap engineering, energy barrier filtering, and texturing will lower the thermal conductivity, optimise carrier concentration, and help in the concurrent improvement in both power factor ($PF = S^2\sigma$) and thermoelectric properties [2, 4, 5, 19].

Among copper chalcogenides, copper sulfides (Cu_xS), where $1 \leq x \leq 2$ are the most rigorously analysed super-ionic conductors. Though they were studied for a long period, only recently, their ability to act efficiently as a mid-high TE material has been studied [12, 13, 20]. With the varying concentration of Cu in Cu_xS , copper sulfides exist in different phases in the following mineral forms: chalcocite (Cu_2S), djurleite ($\text{Cu}_{1.96}\text{S}$), digenite ($\text{Cu}_{1.8}\text{S}$), annilite ($\text{Cu}_{1.75}\text{S}$) and covellite (CuS) [21–25]. Each of them has distinct electrical, optical and structural properties. These multifaceted compositions and crystal structures are the outcomes of the chalcogen's (sulfur) ability to catenate, low electronegative and size difference between Cu and S, and the case that the oxidation number of the chalcogen need not be mandatorily two [14]. Here, the Cu vacancy defects act as acceptors. Thus, they are p-type semiconductors with bandgap energy fluctuating between 1.2 and 1.5 eV [21–24]. This bandgap range makes them a highly desirable choice for solar cells, photocatalysts, field emission devices, nano switches, biosensors and gas sensors [14], and theranostics applications [26].

The primary role of the nanocomposite technique in inducing the energy filtering effect and the reasons for selecting Cu_2S as the host matrix have been briefly discussed in the manuscript. The transition metal oxides are copious and actively sought after for their desirable electrical, optical, and magnetic characteristics [27]. They can be manufactured easily for various applications at cheaper rates. Several

of them (like CuO , ZnO , TiO_2 , and SnO) have prospects of acting as semiconductors. In the semiconductor range, the thermal conductivity due to the charge carriers is, by nature comparatively less [2]. Owing to its wide band gap sweeping from 1.2 to 2.6 eV [28], nanostructured CuO has several applications as in nanofluids, next-generation lithium-ion batteries, photodetectors, supercapacitors, gas and biosensors [29, 30]. Though CuO has high thermal conductivity and low electrical conductivity, this intrinsically p-type semiconductor is chemically stable, can withstand high temperatures and has high mechanical strength. Recently, it has been studied that doping or compositing CuO can act as a promising TE material [31]. The p-type materials are essential in ther-moelectric applications because they complete the thermoelectric couple, enhance the efficiency of thermoelectric devices, enable heat recovery and thermal management, offer design flexibility, and are compatible with commonly used materials. The complementary operation of both p-type and n-type materials is critical for successfully converting heat into electricity and the effective use of thermoelectric technology in various applications.

Amid copper sulfides, cubic chalcocites (Cu_2S) possess highly attractive features in structural and electronic behaviour. Cu_2S is a superionic conductor and fits the Phonon Glass-Electron Crystal (PGEC) notion presented by Slack [32] and extended by Liu et al. [11]. Here, the copper sublattices are formed by the highly mobile Cu cations that can jump easily between different cationic sites, interact with phonons and reduce the thermal conductivity of the material by effectively scattering them. Interestingly, the rigid framework offered by the S atoms (S-fixed in FCC lattice; Cu-interstitial sites), enhances electrical conductivity through proper channelling of the carriers. Thus, the same material behaves as a glass for phonons and a crystal for the charge carriers [2, 5, 13].

The nanocompositing technique has been frequently employed to improve the zT value [33–36]. A classic TE nanocomposite will have a bulk material as its host matrix and nanoparticles as inclusions (on a tiny ratio). It utilizes the energy-filtering mechanism where the newly formed interfaces act as energy barriers and scatter low-energy carriers and phonons at the grain boundaries. To inculcate the earlier stated advantages, Cu_2S was chosen as the host matrix and was composited with broad bandgap metal oxide nanoparticles (CuO , ~2.5 eV). As the physical properties of the inorganic nanostructures are significantly linked with their shape, chemical composition, surface chemistry, crystal structure, and size the method of synthesis becomes critical. Thermally, chemically, and physically stable CuO as nano inclusions into the superionic host matrix Cu_2S with intrinsically high electrical and reduced thermal conductivity. This can effectively balance the relation between the carrier concentration, Seebeck coefficient, and electrical and thermal

conductivity. Hence, the Cu₂S/CuO nanocomposite was selected. Various methods have been proposed to synthesize Cu₂S, including thermolytic, solvothermal, hydrothermal [37], ball-milling [38] and one-pot synthesis [39]. Solvothermal and hydrothermal methods are both techniques used in materials science and chemistry for synthesizing a wide range of materials, including nanoparticles, nanowires, and nanocrystals. These methods offer several advantages: controlled growth, high purity, versatility, efficient reactions, single-step synthesis, property control, green chemistry, scalability, unique structures, and tailored applications. The present work synthesized Cu₂S by solvothermal because it is simple and easily yields single crystals and allows control over particle size at the nanoscale. The transport properties were analysed for the Cu₂S/CuO nanocomposites at varying concentrations. The results correlated with the corresponding crystallographic modifications characterised via powder X-ray diffraction (PXRD), Scanning and Transmission Electron Microscopy (SEM & TEM) and are discussed exhaustively in the coming sessions. In this study, we are reporting the first work based on Cu₂S/CuO nanocomposites to the best of our knowledge.

2 Materials and Methods

2.1 Chemical Precursors

Copper (II) chloride dihydrate (CuCl₂ · 2H₂O, ≥ 99.99%) and thiourea (CH₄N₂S, ≥ 99.99%) were ordered from Sigma Aldrich, India. High-grade polyvinylpyrrolidone (PVP), (C₆H₉NO)_n, ≥ 99.9%), Ethylene Glycol (EG, ≥ 99.8%) ((CH₂OH)₂), liquid ammonium hydroxide (NH₄OH, ≥ 99.9%) and ethanol (C₂H₅OH, ≥ 99%) were ordered from various sources.

2.2 Preparation of Cu₂S Nanoparticles

In the typical synthesis, clear green (Cu) and colourless (S) solutions were obtained by independent mixing of 0.4 M of copper (II) chloride dihydrate and 0.2 M of thiourea in 40 ml of EG, respectively. Before mixing these solutions, 1 g of PVP was added as a capping agent to offer stabilization and prevent the aggregation of nanoparticles. Under continuous stirring, a homogeneous mixture (pastel green) was obtained within 20 min. It was then shifted to a 100 ml Teflon-coated stainless autoclave, sealed, heated at 200 °C for 24 h, and furnace annealed. The final product was taken out and cleansed using deionised water and ethanol multiple times (to remove unreacted ions) and was precipitated under centrifugation. The residue was vacuum dried at 70 °C for 6 h to get a brownish-black powder of Cu₂S.

2.3 Preparation of CuO Nanoparticles

To the stirred solution of 0.2 M of CuCl₂ in 40 ml of distilled water, liquid NH₄OH was added drop by drop till a pH of 9 was achieved. The contents were shifted to an autoclave, heated at 200 °C for 24 h, furnace annealed, and washed with ethanol and deionised water multiple times. The residue was dried in the hot air oven at 70 °C for 6 h to get a greenish-blue powder of CuO. It was finely ground and sintered at 400 °C for 3 h.

2.4 Cu₂S/CuO Nanocomposites (NCs) and Pellet Making

To manufacture composites, sintered CuO nanopowder was mixed with Cu₂S (host) at 0, 5, 10, 15, and 20 weight % ratios, finely ground and kept in a vacuum oven at 300 °C for 12 h within a quartz crucible. Using a cold hydraulic press (5–6 ton pressure), the composite samples were made into circular (13 mm) and rectangular (13 mm × 5 mm × 3 mm) pellets. The pellets were sintered at 300 °C for 3 h.

2.5 Characterization Techniques

The crystal phase studies were recorded by Davinci X-ray powder diffractometer (Bruker D8 Advance USA) with Ni-monochromated Cu-Kα₁ = 1.5406 Å radiation, over the range 20° ≤ 2θ ≤ 70° in steps of 0.0205° at room temperature. The scintillation detector was SSD160 by LYNXEYE, operating at 40 kV and 30 mA. The optical band gap was determined using Ultraviolet–Visible Diffuse Reflectance Spectroscopy (UV–Vis DRS) by Shimadzu UV 3600 PLUS. The thermal behaviour of the Cu₂S/CuO nanocomposite was characterized using the NETZSCH STA 2500 STA2500A-0061-N-Thermogravimetric and differential thermal analyzer (TG/DTA) over a temperature range of RT to 773 K in a controlled atmosphere of N₂. Hi-Resolution Scanning Electron Microscopy (HR-SEM, Thermoscientific Apreo S) and Energy Dispersive X-ray spectroscopy (EDX) were performed to investigate the surface morphology and elemental composition. TEM studies were characterized by Hi-Resolution Transmission Electron Microscope and SAED patterns (HR-TEM, JEOL, JEM-2100 plus, Japan).

2.6 Thermoelectric Measurement

The Seebeck coefficient (*S*) values were recorded from 323 to 573 K in a vacuum using the Seebeck measurement system, Marine India. Between hot and cold junctions, a temperature gradient (Δ*T*) of 50 K was established and its corresponding Seebeck voltage (Δ*V*) was determined according to the expression of $S = -(\Delta V / \Delta T)$. The separation between the two probes utilized in the Seebeck Measurement Technique

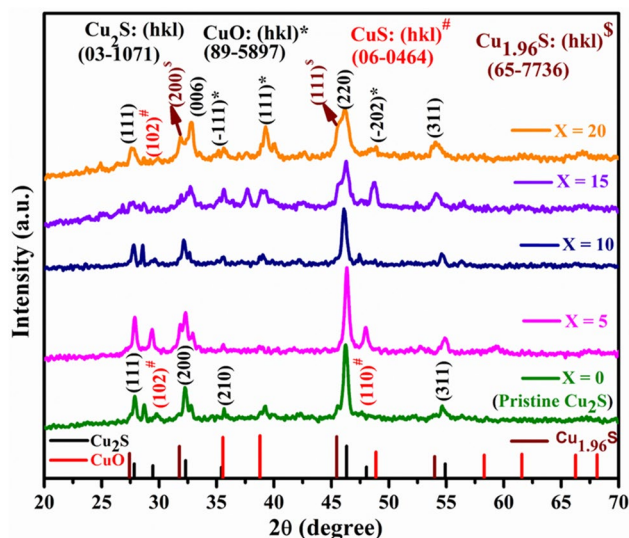


Fig. 1 The powder X-ray diffractograms of $\text{Cu}_2\text{S}/X$ wt% CuO ($X=0, 5, 10, 15,$ and 20 wt%) nanocomposites

is 16 mm. The readings were recorded for every 50 K interval. The thermoelectric Power Factor (PF) was calculated using, $PF = S^2\sigma$. Electrical conductivity (σ) was measured using the standard four-probe Van der Pauw method by the Hall effect measurement system, Excel instruments, India. The Hall effect measurement system (0.5 T and 100 mA) helps in measuring carrier concentration (n) and mobility (μ) as a function of temperature. The separation between the two probes utilized in the Seebeck Measurement Technique is 16 mm. Using a four-probe approach with a constant probe spacing of 1 cm, Hall Measurement was carried out. Thermal diffusivity (λ) and the heat capacity (C_p) were studied under an argon atmosphere using the NETZSCH LFA 467 HT Hyper flash instrument, Germany. The thermal conductivity (κ) was calculated according to $\kappa = \lambda dC_p$, where d is the mass density and was calculated through the Archimedes method.

3 Results and Discussion

3.1 Phase Analysis of $\text{Cu}_2\text{S}/X$ wt% CuO Nanocomposites

The crystal structures and phase purities present in the $\text{Cu}_2\text{S}/X$ wt% CuO ($X=0, 5, 10, 15,$ and 20 wt%) nanocomposites were examined via powder X-ray diffraction (PXRD). The diffractograms were stacked and displayed in Fig. 1. The bottom black curve illustrates the XRD diffractogram of pristine Cu_2S and can be well-indexed to the standard JCPDS No: 03–1071. The diffraction peaks are congruous with a Face-Centered Cubic (FCC) antifluorite

structure (space group: $\text{Fm}\bar{3}\text{m}$) [40]. The primary peaks of Cu_2S that have Bragg's angles at $2\theta = 27.84^\circ, 32.21^\circ, 46.29^\circ,$ and 54.89° correspond to the (111), (200), (220), and (311) planes, respectively.

The strongest reflection at (220) indicates the preferential growth along this direction [41–43]. The (102), (110), (200), and (111) planes indicate the formation of covellite (CuS) JCPDS No: 06-0464 (indicates in # symbols) and djurleite ($\text{Cu}_{1.96}\text{S}$) JCPDS No: 65–7736 (indicates in \$ symbols) as a second phase due to the minor distinction in the enthalpy of formation between Cu_2S and $\text{Cu}_{1.96}\text{S}$ ($\Delta H_f = -79.5$ kJ/mol) and CuS ($\Delta H_f = -53.1$ kJ/mol). The XRD patterns for 5, 10, 15, and 20 wt% CuO samples are also shown in Fig. 1, demonstrating that the CuO nanoparticles are well preserved in all composites. The crystallite size of the pristine sample is 20.85 nm and 5% CuO composite increases to 23.76 nm after that the crystallite size decreases due to the secondary phase of CuS and $\text{Cu}_{1.96}\text{S}$. These secondary phases induce the strain in the crystallite and the grain size is reduced. The peak at (220) is split into two i.e. (220) and (111) after increased composites ratio and the secondary phase of $\text{Cu}_{1.96}\text{S}$. The diffractions planes (–111), (111), (–202), (202), (–311) at $2\theta = 35.56^\circ, 38.78^\circ, 48.87^\circ, 58.30^\circ,$ and 66.25° exactly match with the monoclinic structure of CuO with JCPDS No:89-5897 (space group: $\text{C2}/c$) [44, 45]. The phonon-boundary scatterings are noticeably enhanced by the CuS and $\text{Cu}_{1.96}\text{S}$ impurity phases as well as the grain boundaries formed in the nanocrystals, which dramatically lowers the lattice thermal conductivity [46].

Figure 2a shows the relationship between average crystallite size (D) and lattice parameter (a) in $\text{Cu}_2\text{S}/\text{CuO}$ nanocomposites, where the average D was determined by Scherrer's equation,

$$D = \frac{K\lambda}{\beta \cos\theta} \quad (2)$$

where k (Scherrer's constant) – 0.9, λ – 1.5406 Å, and β — Full-Width Half Maximum (FWHM). From Fig. 2a shows the crystallite (D) value of CuO was calculated as 32.87 nm while for pristine Cu_2S , 20.85 nm and reached its minimum at 20 wt%.

Decreased crystallite/grain size strengthens the grain boundaries, enhancing phonon and low-energy carrier scattering [47]. The crystallite size of the pristine sample is 20.85 nm and 5% CuO composite increases to 23.76 nm after the increase in composite concentration decreases due to the secondary phase of CuS and $\text{Cu}_{1.96}\text{S}$. Figure 2b shows the 3D crystal structure of Cu_2S nano material its consist of blue and red color indicate Cu and S atoms respectively. The interplanar distance (d) was calculated via Bragg's law. The lattice parameters of the FCC Cu_2S were calculated using the,

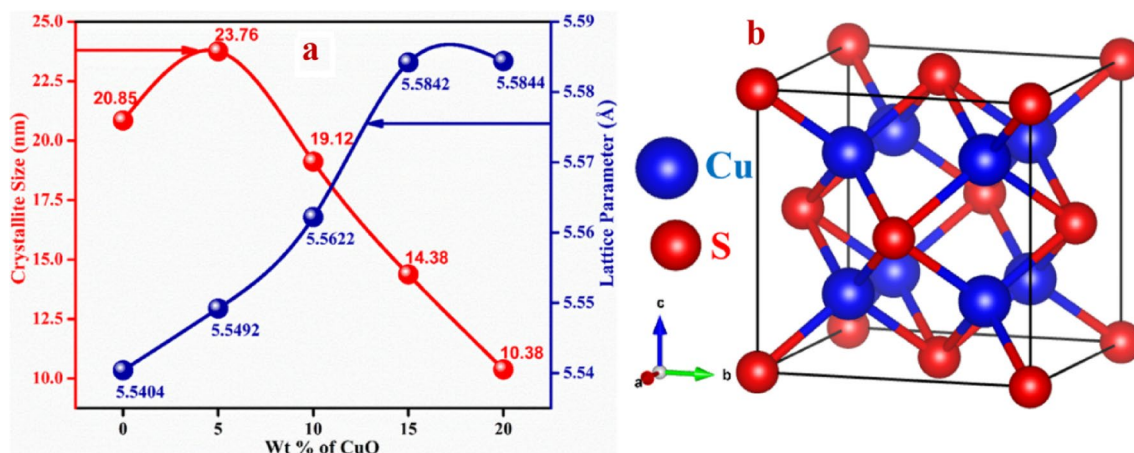


Fig. 2 **a** Crystallite size (*D*) vs lattice parameter of $\text{Cu}_2\text{S}/\text{CuO}$ nanocomposites, **b** 3-D Crystal structure of Cu_2S nanomaterial

$$d = \frac{1}{\sqrt{\frac{h^2}{a^2} + \frac{k^2}{b^2} + \frac{l^2}{c^2}}} \quad (3)$$

While for the monoclinic CuO ,

$$\frac{1}{d^2} = \frac{h^2}{a^2 \sin^2 \beta} + \frac{k^2}{b^2 \sin^2 \beta} - \frac{2hk \cos \beta}{ab \sin^2 \beta} + \frac{l^2}{c^2} \quad (4)$$

The lattice parameters and the crystallographic angles for the pristine Cu_2S and CuO are $a = b = c = 5.5404 \text{ \AA}$; $\alpha = \beta = \gamma = 90^\circ$ and $a = 4.6815 \text{ \AA}$, $b = 3.4216 \text{ \AA}$, $c = 5.1106 \text{ \AA}$; $\alpha = \gamma = 90^\circ$, $\beta = 99.56^\circ$, respectively.

The Cu_2S has a regular calcium Antifluorite structure with a Face-Centred Cubic (FCC) crystal lattice, where the S atoms occupy (0, 0, 0) position and form a rigid framework, which ensures undisturbed motion/flow of electronic carriers through the crystal lattice nodes. Hence, for the charge carriers, the material behaves as a crystal. But the highly mobile copper ions, form the cationic sublattice where they “jump” at very short intervals, resulting in random and strong phonon scattering and reduced thermal conductivity in these materials (comparable to the thermal conductivity of glasses).

3.2 TG–DTA Analysis of $\text{Cu}_2\text{S}/15 \text{ wt\% CuO}$ Nanocomposites

Figure 3 depicts the thermal behaviour of the $\text{Cu}_2\text{S}/15 \text{ wt\% CuO}$ composite. The TGA curve showed a three-stage decomposition under excited temperatures between 30–150 °C, 150–350 °C, and 350–500 °C. The initial weight loss below 150 °C (1.04%) was considered due to the dehydration of distilled water and ethanol used during centrifugation. The second step (<350 °C; 11.82%) was suspected due to the decomposition of PVP (capping agent) and organic compounds such as EG (solvent) used during synthesis.

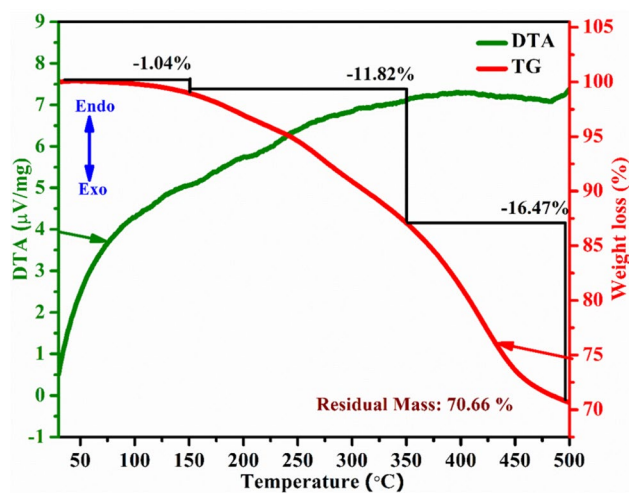


Fig. 3 TG/DTA curves for $\text{Cu}_2\text{S}/15 \text{ wt\% CuO}$ nanocomposite

The major weight loss at the third step of decomposition (<500 °C; 16.47%) can be attributed to the pyrolysis of sulphur in the Cu_2S . Thus, the thermal stability of the Cu_2S is around 300 °C. The exothermic dip in the DTA curve (above 430 °C) confirms the phase transition from $\alpha\text{-Cu}_2\text{S}$ (hexagonal chalcocite) to $\beta\text{-Cu}_2\text{S}$ (cubic chalcocite). No decomposition of CuO was observed, indicating high thermal stability of CuO (above 500 °C) [48, 49]. Hence CuO nanoparticles were sintered at 400 °C. And the composites were sintered at 300 °C.

3.3 Optical Studies of $\text{Cu}_2\text{S}/X \text{ wt\% CuO}$ Nanocomposites

At room temperature, diffuse reflectance studies were carried out over a wavelength range of 200–900 nm. The

optical Bandgap for the $\text{Cu}_2\text{S}/\text{CuO}$ composites was estimated through Tauc plots, by using the equation,

$$(\alpha h\nu)^n = A(h\nu - E_g) \quad (5)$$

where α , h , ν , A and E_g are the absorption coefficient, Planck's constant, photon frequency, the proportionality constant and Bandgap energy. Depending on whether the transition is direct or indirect, n can be $\frac{1}{2}$ or 2 . As the linearity was well-kept for $n=2$, $(\alpha h\nu)^2$ vs eV graph was plotted and extrapolated over the linear portion of the curve to find E_g [50]. From Fig. 4a–e, the E_g has been determined to be 1.7 eV, 1.9 eV, 2.0 eV, 2.1 eV and 2.2 eV for $X=0, 5, 10, 15$ and 20 wt% composites, respectively. The value of 1.7 eV matched the literature [51, 52]. Reportedly, the bulk phase of Cu_2S has an absorption peak in the Near Infra-Red region (1022 nm, 1.21 eV) [52–55]. However, the Cu_2S nanoclusters show clear absorption below 350 nm.

The observed blue shift can plausibly be the consequence of the quantum size effect [52, 55].

The increase in E_g with the increasing wt% of CuO can be attributed to the following factors: (i) With increasing wt% of CuO, particle size decreases, resulting in increased surface area and effective absorption at the molecular level [56], (ii) Appreciable electronegative difference [57], (iii) As seen in Fig. 4f, CuO has strong absorption in the visible region with an absorption edge at 510 nm ($E_g = 2.5$ eV) [58]. This wide band gap will further distance the valence band from the conduction band. Thus, compositing CuO nanoparticles in the Cu_2S matrix helps in tuning the band gap. The introduced energy barrier will aid in the low-energy carrier and phonon filtering, which can simultaneously improve the Seebeck coefficient and lower the lattice thermal conductivity [59].

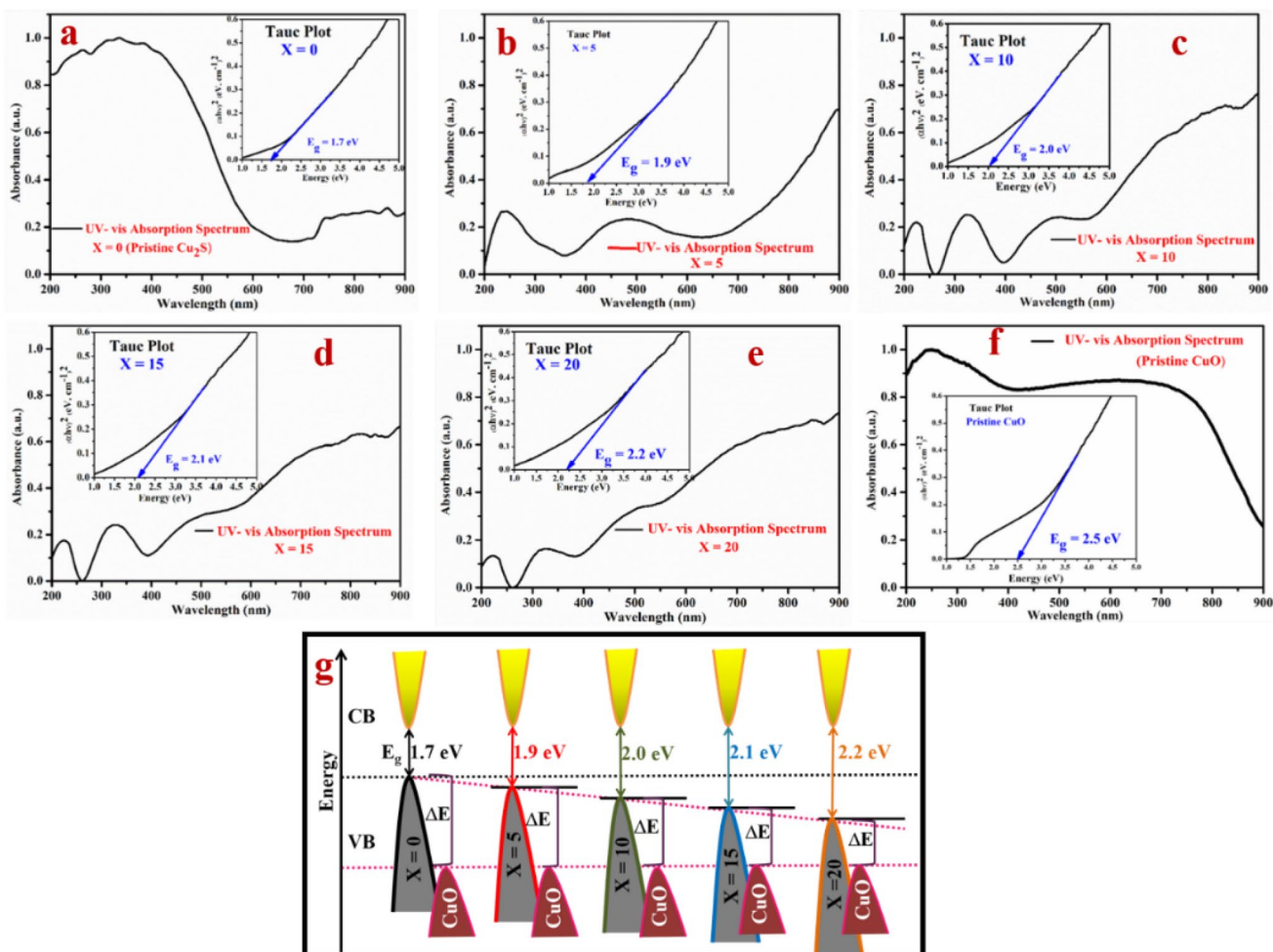


Fig. 4 a–e UV–vis Absorbance spectra and Tauc plots for the $\text{Cu}_2\text{S}/X$ wt% CuO ($X=0, 5, 10, 15$, and 20 wt%) nanocomposites, f Pristine CuO and g Scheme of Band Structure

3.4 Microstructural Analysis of Cu₂S/X wt% CuO Nanocomposites

Figure 5a and b show the surface morphology of low and high-magnification images of the pristine Cu₂S sample. It can be seen that at the microscale level, the Cu₂S nanoparticles were homogeneously dispersed. The high-magnification image revealed that the particles were more likely to be rigid and spherically shaped. The formation of particles with average 70–90 nm diameters was measured. The microstructural features changed apparently with increasing wt% of CuO nanoparticles in the Cu₂S matrix.

As shown in Fig. 6a and b, for the 5 wt% sample, many of the particles lost their spherical shape to some extent and became coarse. This was evidently due to the formation of new CuO interfaces. The same was in the case of the 20 wt% sample shown in Fig. 7a and b, where the spherical nature of the particle was utmostly lost. Also, the particle size reduced with increasing X values. This can strengthen grain boundaries and help optimise the Seebeck coefficient and lattice thermal conductivity values by effective scattering. While the elemental mapping images shown in Figs. 5c–e, 6 and 7c–f ensured the homogenous dispersion of all individual elements, the composition of these elements was identified through the EDX analysis which is shown in inset of Figs. 5f and 6g. The 2:1 atomic ratio of Cu and S atoms certified the formation of a high-grade Chalcocite (Cu₂S). The EDX spectra of the

composites also verified the presence and percentage of Cu, S and O nanoparticles and are shown in Figs. 5f, 6g, and 7g. No other impurities were found and the percentage of Cu is increased while adding CuO nanoparticles to the Cu₂S matrix. There is no noticeable change in sulphur percentage due to the addition of CuO.

The HR-TEM analysis from Figs. 8 and 9a, b, and c of the pristine Cu₂S nanostructure and Cu₂S/15 wt% CuO composite confirmed the distribution of CuO nanoparticles (NPs) in the Cu₂S matrix. The darker areas in the HR-TEM micrographs are the diffraction contrast difference induced by the nano inclusion of CuO particles. As they are denser, only fewer beam electrons can transmit through. These CuO regions will act as filtering/scattering centres for phonons and low-energy charge carriers [60]. The lattice d-spacing calculations were done using the ImageJ software. The d values of 0.31 nm correspond to the (111) plane of the cubic Cu₂S (03-1071) show in Fig. 8c. Figure 9c shows the d values of 0.32 nm and 0.26 nm correspond to the (111) plane of the cubic Cu₂S (03-1071) and the (-111) plane of the monoclinic CuO (89-5897), respectively. The inset images unveil the highly crystalline lattice fringes. Figures 8d and 9d shows the Selected Area Electron Diffraction (SAED) pattern of the composite. The presence of the (111), (220), and (311) lattice planes was consistent with the XRD diffraction peaks. The SAED pattern further displays the polycrystalline nature of the composite.

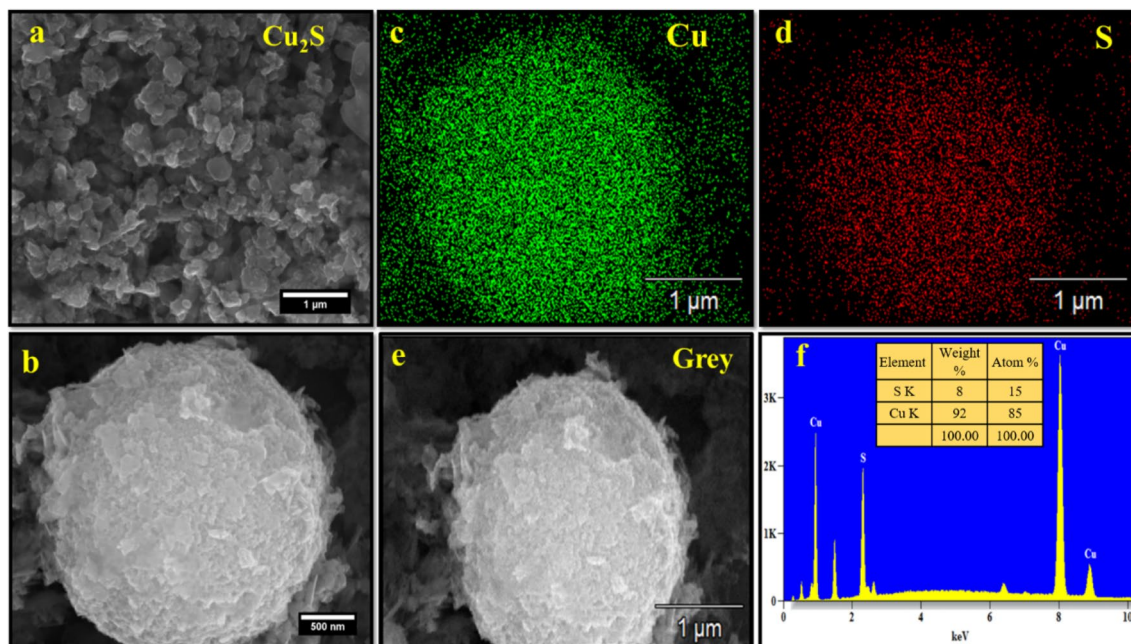


Fig. 5 HR-SEM images (a, b) elemental mapping, grey image (c, d, e) and EDX spectrum (f) of pristine Cu₂S nanostructure (inset weight percentage of selected elements)

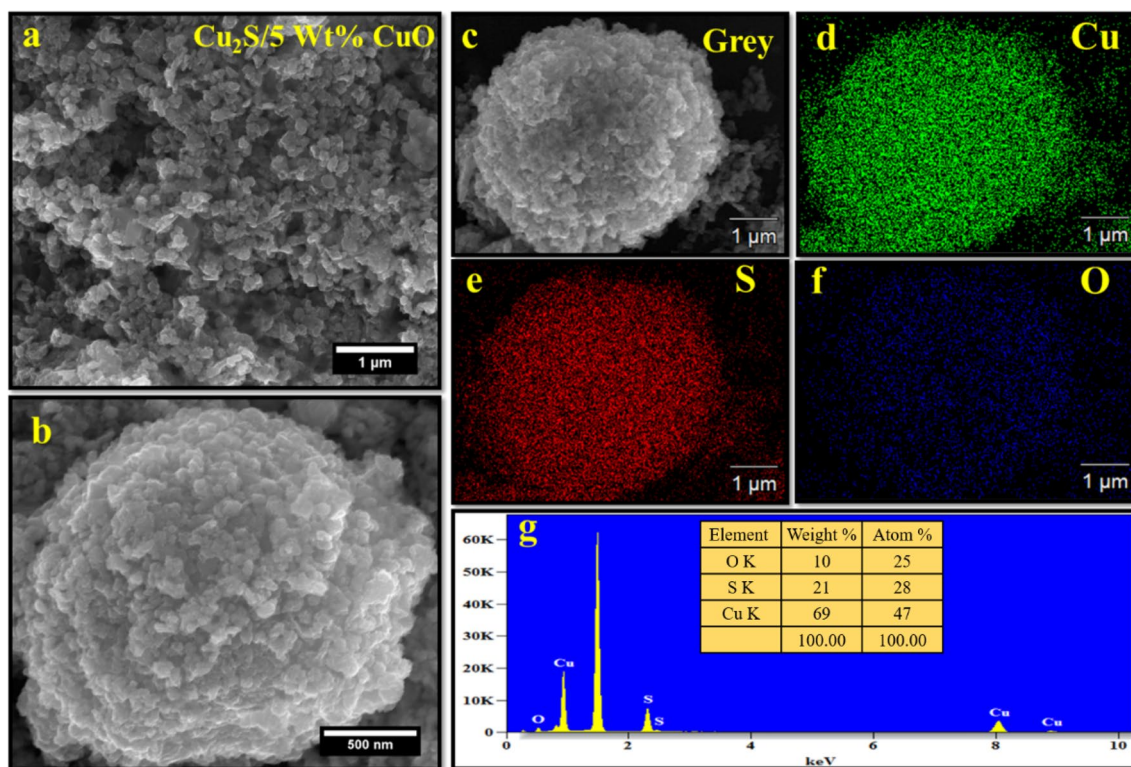


Fig. 6 a, b HR-SEM images, c–f elemental mapping, and g EDX spectrum of the $\text{Cu}_2\text{S}/5$ wt% CuO composite (insite weight percentage of selected elements)

4 Thermoelectric Properties of $\text{Cu}_2\text{S}/X$ wt% CuO Nanocomposites

Figure 10a shows the temperature dependence of the Seebeck coefficient (S) for $\text{Cu}_2\text{S}/X$ wt% CuO ($X=0, 5, 10, 15,$ and 20 wt%) nanocomposites (NCs) over the range 323 K to 573 K. The positive values indicate that the pure Cu_2S and its composites with CuO have holes as their majority charge carriers exhibiting p-type semiconductor nature. This can be attributed to the low chemical potential of Cu, which increases the thermodynamic propensity of superionic chalcocite towards copper vacancies [61, 62]. With increasing temperature, the Seebeck coefficient of all wt % NCs increased monotonically.

The S value of the pure Cu_2S at 323 K was $75.39 \mu\text{VK}^{-1}$, but after the dispersion of $5, 10, 15$ and 20 wt% CuO nanoparticles, the S value increased to $91.39 \mu\text{VK}^{-1}$, $127.81 \mu\text{VK}^{-1}$, $138.21 \mu\text{VK}^{-1}$ and $182.91 \mu\text{VK}^{-1}$ respectively, which is a maximum of 142.62% increase at 323 K. Also, from Fig. 10a, it is interesting to notice that these hybrids ($5, 10, 15,$ and 20 wt% CuO samples) exhibit very close changes in their values over the entire temperature range, indicating that they are stable thermoelectric materials. The increment in S values with CuO addition was more pronounced at higher temperatures and had a maximum

value of $271.86 \mu\text{VK}^{-1}$ at 573 K for the 20 wt% sample. This is a 71.45% improvement from the pure Cu_2S sample ($158.57 \mu\text{VK}^{-1}$) at the same temperature. The enhanced S values can be predicted due to the energy filtering of holes by introducing potential barriers with an appropriate band gap in the form of interfaces. This restricts the low-energy carriers entering a material [63–65].

Figure 10b shows the temperature dependence of electrical conductivity (σ) of pure Cu_2S and $\text{Cu}_2\text{S}/\text{CuO}$ composites of varying concentrations. Unlike the Seebeck coefficient, the electrical conductivity decreased with increasing wt% of CuO. At 323 K, the pure Cu_2S has an electrical conductivity of 2.5×10^4 S/m, close to the reported value [66]. This was reduced to 2.1×10^4 S/m, 1.4×10^4 S/m, 1.2×10^4 S/m and 0.6×10^4 S/m by the dispersion of $5, 10, 15,$ and 20 wt % of CuO in Cu_2S matrix. The decline in the σ values was expected as the E_g increased with the increasing wt% of CuO. The σ values improved with the increase in temperature, indicating a typical semiconductor behaviour. The electrical conductivity of a semiconductor depends on its n and μ values, where the relation is given by $\sigma = n\mu e$. From the analysis of n, μ and σ values, it can be seen that the reduction in n values plays a dominant role in the reduction of σ values irrespective of the enhancement found in μ values with increasing wt% of CuO in $\text{Cu}_2\text{S}/\text{CuO}$ composites. Thus,

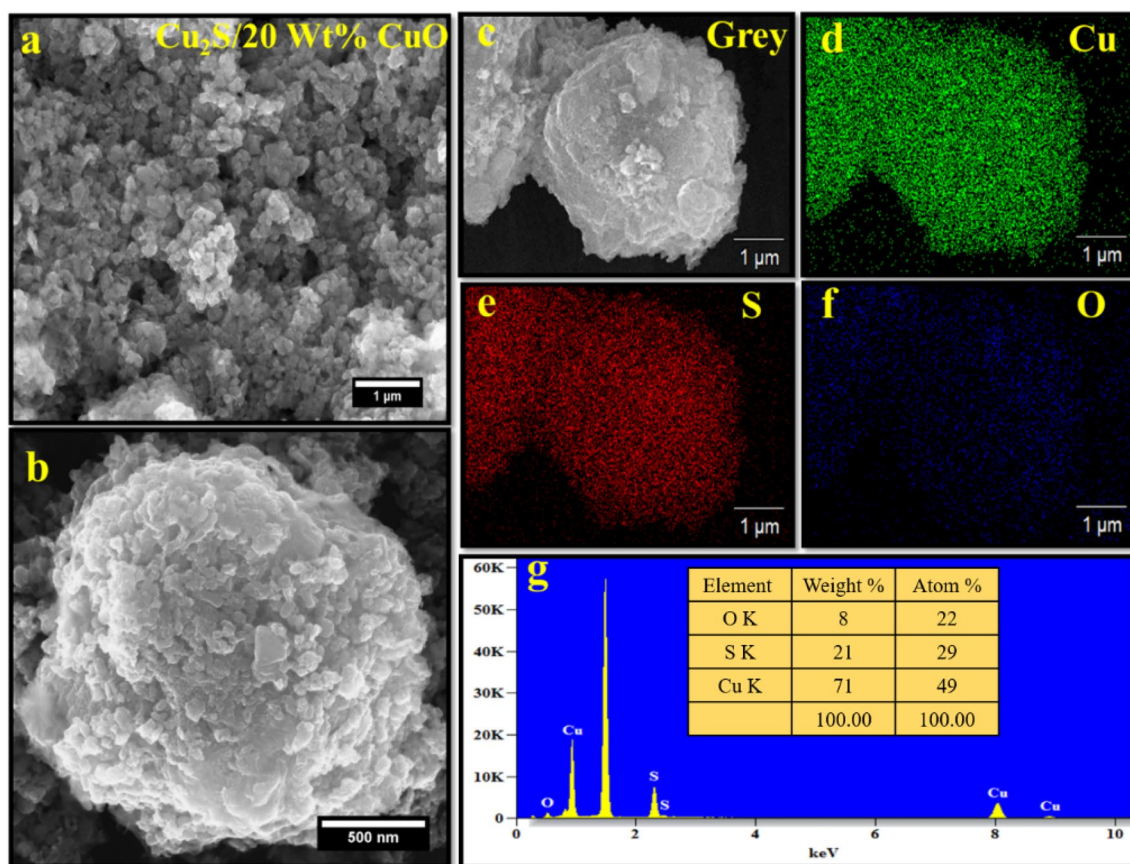


Fig. 7 a, b HR-SEM images, c–f elemental mapping, and g EDX spectrum of the $\text{Cu}_2\text{S}/20$ wt% CuO composite (insite weight percentage of selected elements)

the band gap mismatch plays an important role in carrier transport properties. These results were also consistent with the electrical testing.

Figure 10c illustrates the schematic representation of low-energy hole filtering at an interfacial boundary between the Cu_2S matrix and CuO nanoparticles. Thus, up to 15 wt% of CuO addition, the S values have increased with decreasing n values, thus obeying the Pisarenko relation for semiconductors,

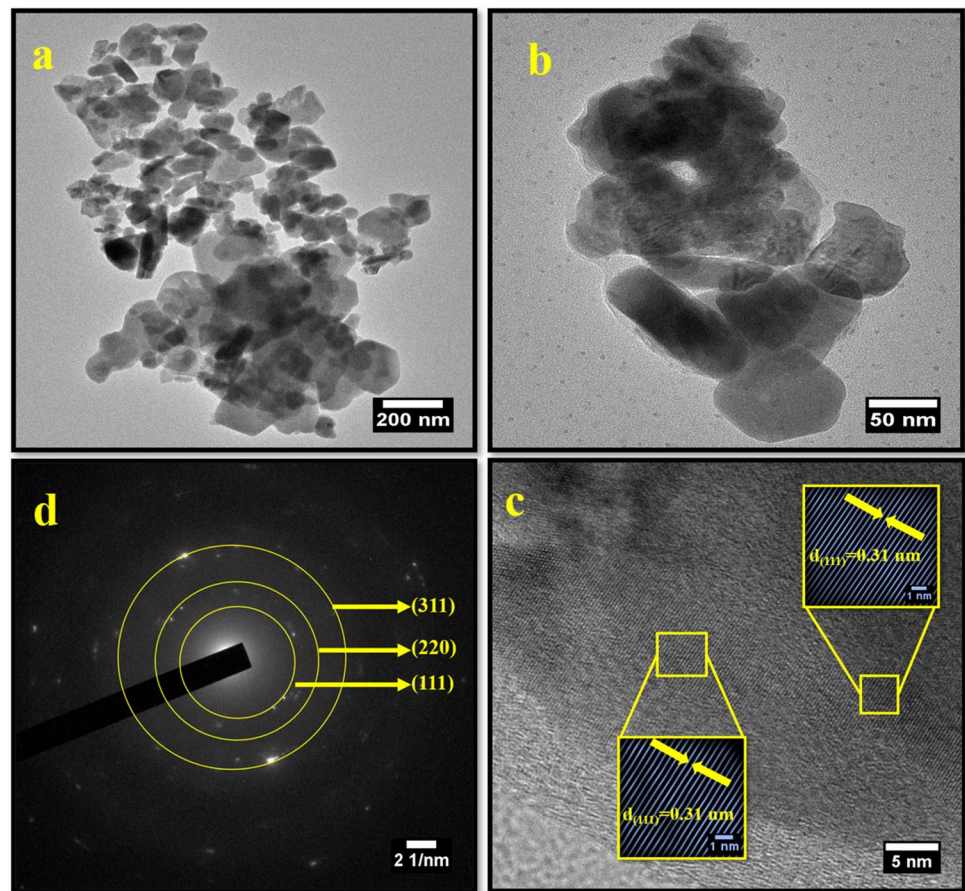
$$S = \frac{8\pi^2 k_b^2 T}{3eh^2} m^* \left(\frac{\pi}{3n} \right)^{\frac{2}{3}} \quad (6)$$

where S —the Seebeck coefficient ($\mu\text{V K}^{-1}$), k_b —the Boltzmann constant ($1.3806 \times 10^{-23} \text{ m}^2 \text{ kg s}^{-2} \text{ K}^{-1}$), T —Absolute temperature (K), m^* —the effective mass, h —the Planck's constant ($6.6261 \times 10^{-34} \text{ J.s}$), e —the electronic charge ($1.6021 \times 10^{-19} \text{ C}$), and n —the carrier concentration (cm^{-3}). This proves that 15 wt% is the ideal amount for CuO dispersion in the Cu_2S matrix to achieve effective energy filtering. As discussed by Pakdel et al., the addition of nanoparticles (inclusions) beyond a certain wt% can lead to a distribution

of large amounts of nanoparticles in the grain boundaries of the host matrix [67]. The same was also confirmed in the SEM analysis. These agglomerations will affect the effective energy-filtering mechanism, thus resulting in increased S values up to 20 wt% sample. However, all the hybrid samples exhibited enhanced Seebeck coefficient values when compared to the pure Cu_2S sample.

The increasing trend verified negligible minority carriers' contribution even at elevated temperatures. It is evident from Fig. 10a that the addition of CuO nanoparticles has markedly improved the Seebeck coefficient for $\text{Cu}_2\text{S}/\text{CuO}$ NCs, which was consistent with decreasing carrier concentration. Table 1 provides the temperature dependence data of carrier concentration (n) and mobility (μ) for all samples. Understanding the band structure is crucial for analysing obtained Seebeck coefficient values. With increasing wt% of CuO, the decreased n is due to the broadened E_g gap. The n values increase with temperature as it is more likely for the carriers to jump from the Valence Band (VB) to the Conduction Band (CB). The decrement in the μ values proves solid phonon scattering with the increase in temperature [68]. Figure 7d establishes the inverse relation between n and μ . But

Fig. 8 **a, b**, TEM and **c** HR-TEM images, **d** SAED pattern of the pristine Cu_2S nanostructure



beyond 15 wt%, since fine grains can scatter severely the mobility decreases sharply. When the grain size becomes effectively small, it strengthens the grain boundaries and increases carrier and phonon scattering [69, 70].

The Power Factor ($\text{PF} = S^2\sigma$) was determined to examine the competence of electronic transport in TE materials. The temperature dependence of $\text{Cu}_2\text{S}/\text{CuO}$ composites is shown in Fig. 11. The PF has been enhanced predominantly by CuO compositing, especially for the 15 wt% sample. Also, the PF shows a decreasing trend with increasing wt% of CuO dispersion; this signifies the dominance of electrical conductivity over the Seebeck coefficient. For all the samples, the PF showed pronounced improvement at the higher temperatures, which confirms the characteristic of copper chalcogenides shifting towards a more ordered phase at higher temperatures, as discussed earlier. Among all the samples, the 15 wt% samples achieved the maximum PF value of $952.66 \mu\text{Wm}^{-1} \text{K}^{-2}$ at 573 K, which was 32.23% greater than pure Cu_2S ($720.44 \mu\text{Wm}^{-1} \text{K}^{-2}$) at the same temperature. The $720.44 \mu\text{Wm}^{-1} \text{K}^{-2}$ value was close to the earlier reported value [66]. This enhancement is greater

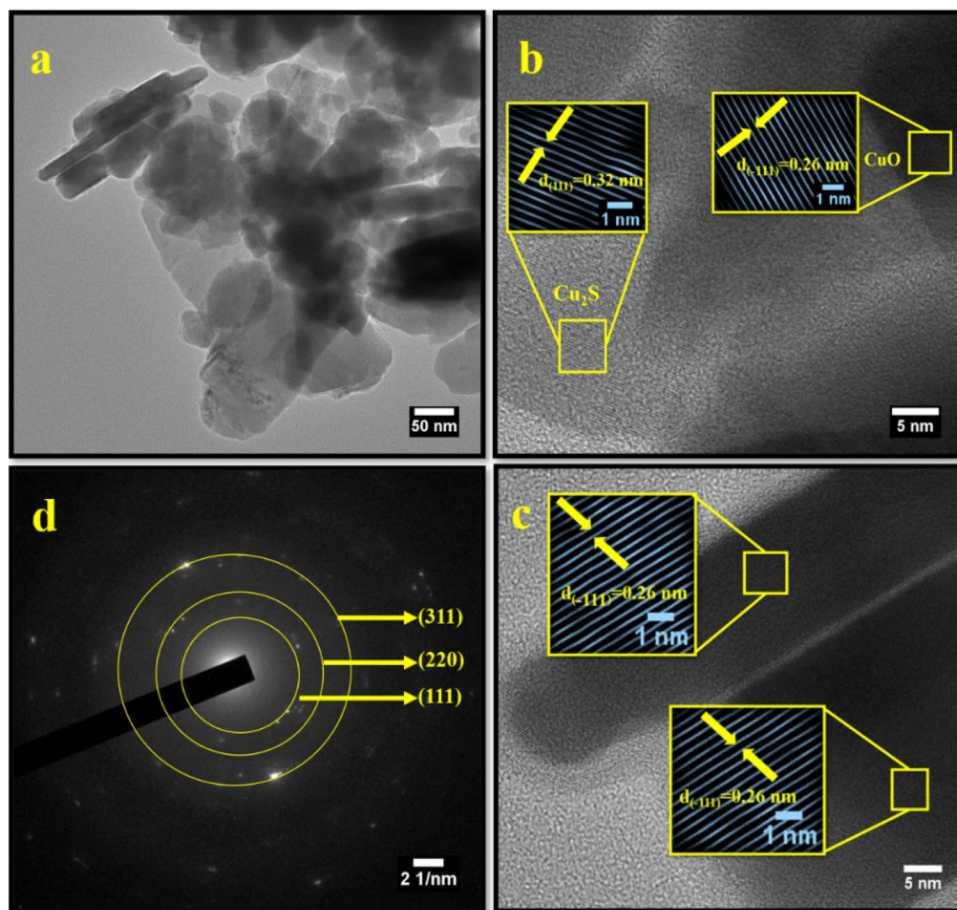
than previously reported works based on Cu_2S -based thermoelectric materials carried out by different groups [66, 71–76]. Such a high PF value is desirable from the point of view of low-cost, less toxic, practical and sustainable power generation.

Figure 12 highlights that we have achieved a significant decrement in the thermal conductivity values without compromising the improvement in the PF values, thus resulting in high zT values. The total thermal conductivity (κ_T) is the algebraic addition of the electronic (κ_e) (Fig. 12b), lattice (κ_l) (Fig. 12c) and contributions. The Lorenz Number for the materials with experimental Seebeck coefficient values can be calculated by the relation shown in Eq. (7), where, S is the Seebeck coefficient.

$$L_0 = 1.5 + \exp\left[-\frac{|S|}{116}\right] \quad (7)$$

From Fig. 12b, the Lorenz value is decreased with increasing temperature and increased with increasing CuO concentration. It is decreased from $1.8643 \times 10^{-8} \text{W}\Omega/\text{K}^2$

Fig. 9 **a** TEM image, **b, c** HR-TEM images, **d** SAED pattern of the $\text{Cu}_2\text{S}/15 \text{ wt\% CuO}$ nanocomposite



to $1.6517 \times 10^{-8} \text{ W}\Omega/\text{K}^2$ at 573 K. And from the Wiedemann–Franz law, $\kappa_e = L_0 \sigma T$ (L_0 is the Lorenz number, $1.6 \times 10^{-8} \text{ V}^2\text{K}^{-2}$), the phononic contribution was calculated by, $\kappa_L = \kappa_T - \kappa_e$. The κ_T values were notably reduced from $2.97 \text{ Wm}^{-1} \text{ K}^{-1}$ (pristine Cu_2S) to $1.92 \text{ Wm}^{-1} \text{ K}^{-1}$, $1.52 \text{ Wm}^{-1} \text{ K}^{-1}$, $1.24 \text{ Wm}^{-1} \text{ K}^{-1}$ and $1.14 \text{ Wm}^{-1} \text{ K}^{-1}$ for the 5, 10, 15 and 20 wt% CuO samples which is almost a 61.62% reduction at 573 K shown in Fig. 12a. The reduction in the κ_T could be due to the combined effect of (i) a prominent increase in phonon-grain boundary scatterings, which ultimately leads to a lessened mean free path for phonons ($\therefore \kappa_L \downarrow$) and (ii) the hot carriers' scatterings at the introduced interfaces ($\therefore \kappa_e \downarrow$).

Overall, the $\text{Cu}_2\text{S}/\text{CuO}$ composite samples exhibited improved figure of merit (zT) values when compared to pristine Cu_2S (Fig. 13a) owing to improved PF and reduced κ_T . Also, the zT values have sharply increased with the temperature. This is due to the change towards the more ordered phases, thus exhibiting the very nature of copper chalcogenides. At 573 K, the $\text{Cu}_2\text{S}/15 \text{ wt\% CuO}$ sample achieved the most optimised zT value of 0.44, a 214.29%

gain compared to the pure Cu_2S sample with a zT value of 0.14 [66]. Figure 13b displays the comparative bar graph of thermoelectric parameters like S , σ , PF, κ and zT at 573 K. It is evident from the comparison graph that the excellent TE performance exhibited by sample $\text{Cu}_2\text{S}/15 \text{ wt\% CuO}$ results from both increased power factor (dominated by the increase of S by energy filtering of carriers) and reduced thermal conductivity (achieved through interface scattering of phonons and carriers at grain boundaries).

5 Conclusion

In essence, the Cu_2S and CuO nanopowders were prepared via Solvothermal and Hydrothermal methods, respectively. They were manually mixed and ground at precise ratios to fabricate highly standard $\text{Cu}_2\text{S}/X \text{ wt\% CuO}$ nanocomposites. The XRD studies verified the antifluorite (FCC) and monoclinic crystal structures of Cu_2S and CuO samples. The HR-SEM and HR-TEM micrograms revealed the nanocluster morphology of the composites, confirmed

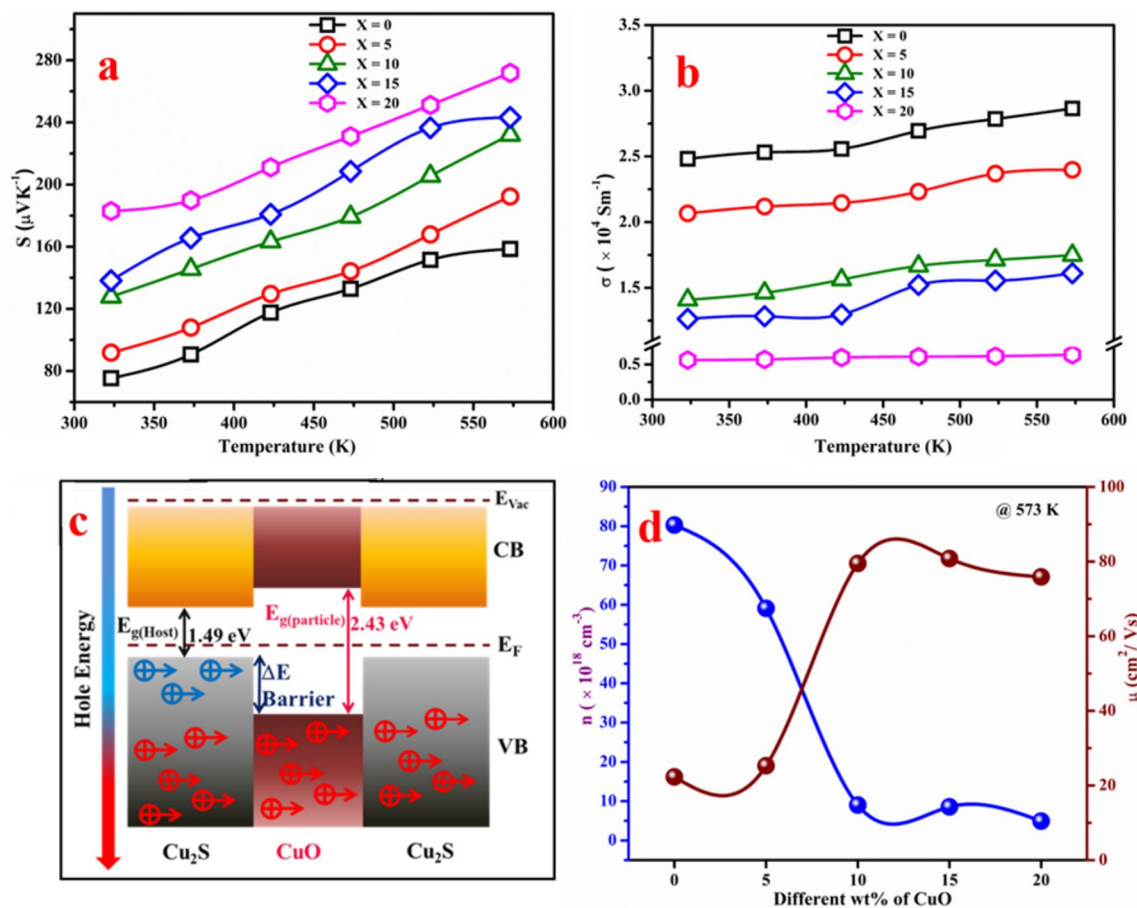


Fig. 10 **a** and **b** Temperature dependence of Seebeck coefficient and electrical conductivity in $\text{Cu}_2\text{S}/X$ wt% CuO nanocomposites, **c** A schematic representation of low energy carrier filtering, and **d** Relation between carrier concentration and Hall mobility as a function of

X at 573 K. Open black squares, open red circle, open green triangles, open blue diamonds, and open pink hexagonal represents $X=0, 5, 10, 15,$ and 20 wt%, respectively (Color figure online)

Table 1 Carrier concentration and Hall mobility of $\text{Cu}_2\text{S}/\text{CuO}$ nanocomposites as a function of temperature

Temp. (K)	Carrier concentration (n) (10^{18} cm^{-3})					Mobility (μ) (cm^2/Vs)				
	X=0	X=5	X=10	X=15	X=20	X=0	X=5	X=10	X=15	X=20
323	41.9	12.8	6.21	4.57	2.45	36.9	101	238	293	155
373	54.9	14.0	7.30	4.81	3.18	33.8	94.8	217	249	121
423	56.3	21.3	7.90	5.68	3.48	30.9	80	202	239	114
473	62.3	47.5	8.12	6.29	4.01	28.2	69.3	99.1	226	87.5
523	79.8	52.4	8.75	7.57	4.32	25.4	48.2	89.8	224	82.7
573	80.3	59.1	9.02	8.55	4.93	22.3	25.3	79.5	222	75.9

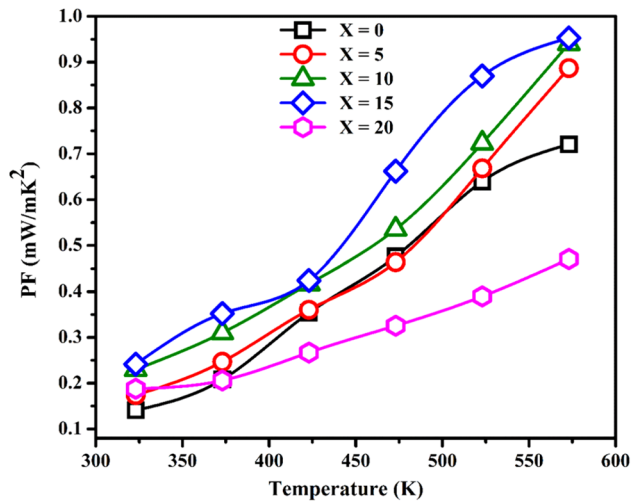


Fig. 11 Temperature dependence Power Factor of $\text{Cu}_2\text{S}/X$ wt% CuO ($X=0, 5, 10, 15,$ and 20 wt%) nanocomposites

the particle size reduction effect due to compositing, and unveiled the homogeneous incorporation of CuO nanoparticles in the Cu_2S matrix with no impurity elements. From the optical absorption characteristics, the blue shift in the absorption edge wavelengths of the composites was observed with an increase in wt% of CuO nanoparticles. The fundamental changes in their size, structure, morphology and optical bandgap values were well reflected in the experimental results. The newly formed CuO interfaces and strengthened grain boundaries enhanced the Seebeck coefficient and diminished thermal conductivity values. The above-stated factors positively impacted our combined strategy of carrier filtering and phonon scattering and yielded a very high PF value of $952.66 \mu\text{Wm}^{-1} \text{K}^{-2}$ (32.23% gain) for the $\text{Cu}_2\text{S}/15$ wt% CuO sample and an efficient zT value of 0.44 (214.29% gain) for the $\text{Cu}_2\text{S}/15$ wt% CuO at 573 K. The current study may be applied to different TE materials to optimise their thermoelectric and transport characteristics. TE materials with such high PF and zT values will make the real-time application of direct conversion devices feasible.

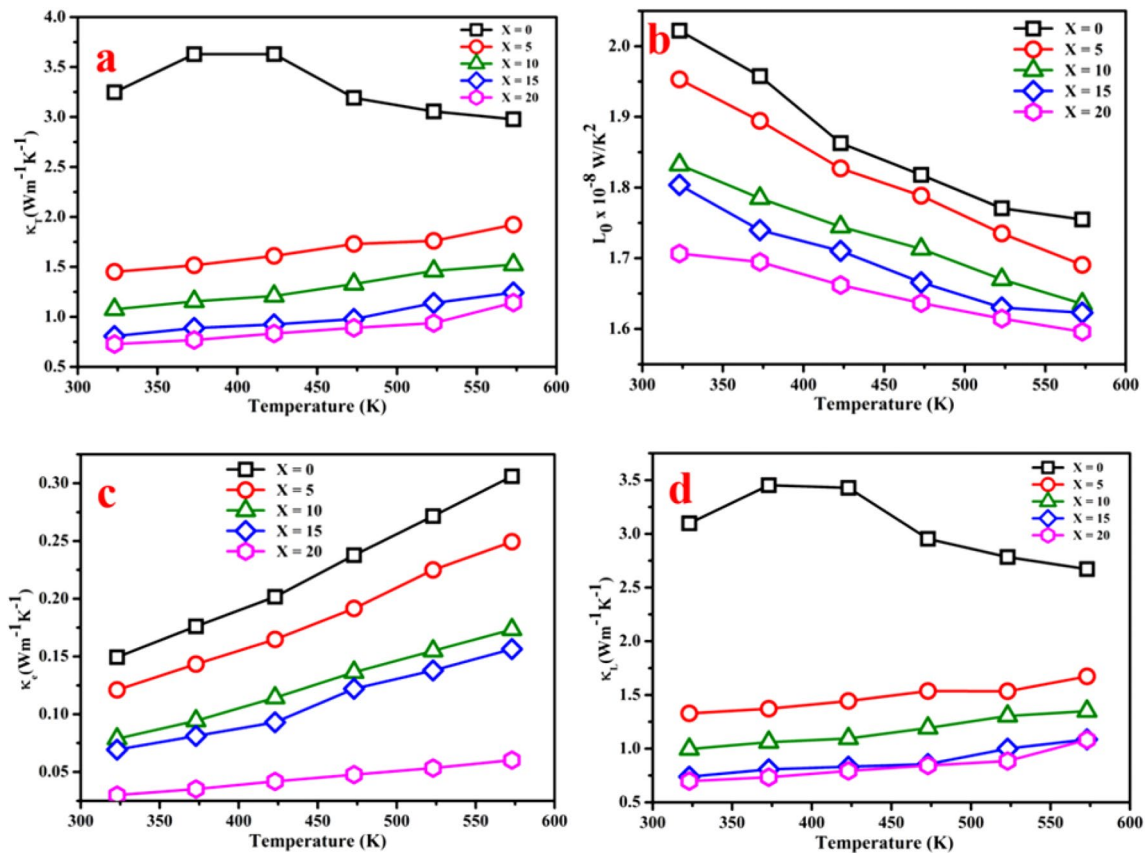


Fig. 12 Temperature dependence of **a** Total (κ_T) thermal conductivities, **b** Lorentz number (L_0), **c** Electronic (κ_e) and **d** Lattice (κ_L) thermal conductivities of $\text{Cu}_2\text{S}/X$ wt% CuO ($X=0, 5, 10, 15,$ and 20 wt%) nanocomposites

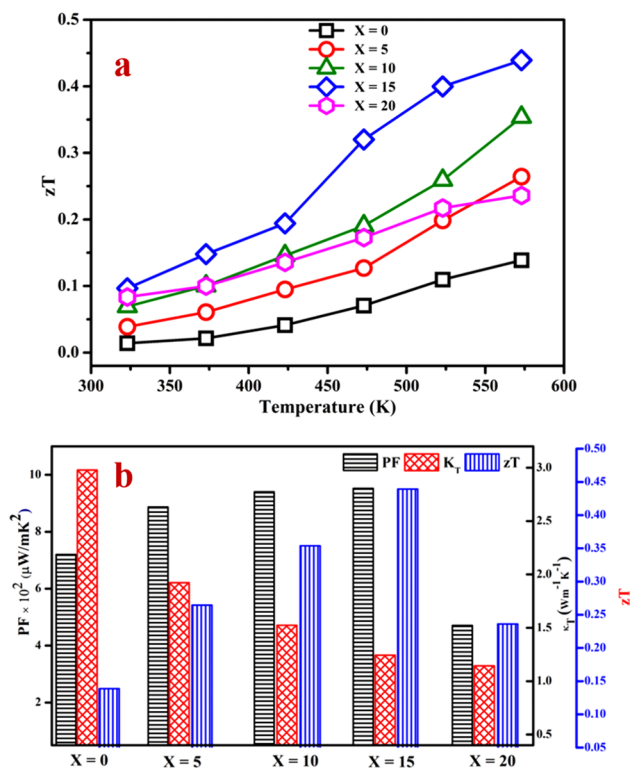


Fig. 13 **a** Figure of Merit (zT) values and **b** Comparative bar graph of TE parameters: Seebeck coefficient, Electrical conductivity, Power factor, Thermal conductivity, and Figure of merit of all the samples at 573 K

Author contributions JM: performed writing-original drafts, investigations, and conceptualization. SR and RR: performed an investigation and writing methodology. FJP: performed plots and validation formal analysis. MA: performed investigation, resources, and data curation. GA: performed supervision, review and editing, and project administration. All authors have read and agreed to the published version of the manuscript.

Funding The authors declare that no fundings or other supports received for the reported work.

Declarations

Competing interests The authors declare no competing interests.

References

- G.J. Snyder, E.S. Toberer, Complex thermoelectric materials, in *Materials for sustainable energy: a collection of peer-reviewed research and review articles from Nature Publishing Group*. (World Scientific, 2011), pp.101–110
- Z.-G. Chen et al., Nanostructured thermoelectric materials: current research and future challenge. *Prog. Nat. Sci. Mater. Int.* **22**(6), 535–549 (2012)
- Y. Pei et al., Stabilizing the optimal carrier concentration for high thermoelectric efficiency. *Adv. Mater.* **23**(47), 5674–5678 (2011)

- C. Zhao et al., Defects engineering with multiple dimensions in thermoelectric materials. *Research.* **2020**, 9652749 (2020)
- T.M. Tritt, Thermoelectric phenomena, materials, and applications. *Annu. Rev. Mater. Res.* **41**(1), 433–448 (2011)
- X. Zhang, L.-D. Zhao, Thermoelectric materials: energy conversion between heat and electricity. *J. Materiomics* **1**(2), 92–105 (2015)
- H. Mamur et al., A review on bismuth telluride (Bi₂Te₃) nanostructure for thermoelectric applications. *Renew. Sustain. Energy Rev.* **82**, 4159–4169 (2018)
- G. Ding et al., High thermoelectric properties of n-type Cd-doped PbTe prepared by melt spinning. *Scr. Mater.* **122**, 1–4 (2016)
- G. Zheng et al., Toward high-thermoelectric-performance large-size nanostructured BiSbTe alloys via optimization of sintering-temperature distribution. *Adv. Energy Mater.* **6**(13), 1600595 (2016)
- B. Ge et al., Atomic level defect structure engineering for unusually high average thermoelectric figure of merit in n-type pbse rivalling PbTe. *Adv. Sci. (Weinh.)* **9**, 2203782 (2022)
- H. Liu et al., Ultrahigh thermoelectric performance by electron and phonon critical scattering in Cu₂Se_{1-x}I_x. *Adv. Mater.* **25**(45), 6607–6612 (2013)
- W.D. Liu et al., Promising and eco-friendly Cu₂X-based thermoelectric materials: progress and applications. *Adv. Mater.* **32**(8), 1905703 (2020)
- K. Zhao et al., Recent advances in liquid-like thermoelectric materials. *Adv. Funct. Mater.* **30**(8), 1903867 (2020)
- C. Coughlan et al., Compound copper chalcogenide nanocrystals. *Chem. Rev.* **117**(9), 5865–6109 (2017)
- M. Bouroushian, *Chalcogens and metal chalcogenides, in electrochemistry of metal chalcogenides* (Springer, 2010), pp.1–56
- J.B. Rivest et al., Size dependence of a temperature-induced solid-solid phase transition in copper (I) sulfide. *J. Phys. Chem. Lett.* **2**(19), 2402–2406 (2011)
- W.R. Cook, *Phase changes in Cu₂S as a function of temperature* (National Bureau of Standards, 1972)
- K. Okamoto, S. Kawai, Electrical conduction and phase transition of copper sulfides. *Jpn. J. Appl. Phys.* **12**(8), 1130 (1973)
- D. Singh, R. Ahuja, Dimensionality effects in high-performance thermoelectric materials: computational and experimental progress in energy harvesting applications. *Wiley Interdiscip. Rev. Comput. Mol. Sci.* **12**(1), e1547 (2022)
- G. Dennler et al., Are binary copper sulfides/selenides really new and promising thermoelectric materials? *Adv. Energy Mater.* **4**(9), 1301581 (2014)
- R. Potter, An electrochemical investigation of the system copper-sulfur. *Econ. Geol.* **72**(8), 1524–1542 (1977)
- G. Will, E. Hinze, A.R.M. Abdelrahman, Crystal structure analysis and refinement of digenite, Cu_{1.8}S, in the temperature range 20 to 500 C under controlled sulfur partial pressure. *Eur. J. Mineral.* **14**(3), 591–598 (2002)
- H.T. Evans, The crystal structures of low chalcocite and djurleite. *Zeitschrift für Kristallographie-Crystalline Materials* **150**(1–4), 299–320 (1979)
- K. Koto, N. Morimoto, The crystal structure of anilite. *Acta Crystallogr. Sect. B Struct. Crystallogr. Cryst. Chem.* **26**(7), 915–924 (1970)
- V.I. Klimov, V.A. Karavanskii, Mechanisms for optical nonlinearities and ultrafast carrier dynamics in Cu_xS nanocrystals. *Phys. Rev. B* **54**(11), 8087 (1996)
- S. Goel, F. Chen, W. Cai, Synthesis and biomedical applications of copper sulfide nanoparticles: from sensors to theranostics. *Small* **10**(4), 631–645 (2014)
- Q. Zhang et al., CuO nanostructures: synthesis, characterization, growth mechanisms, fundamental properties, and applications. *Prog. Mater. Sci.* **60**, 208–337 (2014)

28. Y. Wang et al., Fabrication of nanostructured CuO films by electrodeposition and their photocatalytic properties. *Appl. Surf. Sci.* **317**, 414–421 (2014)
29. S. Wang et al., A CuO nanowire infrared photodetector. *Sens. Actuators A Phys.* **171**(2), 207–211 (2011)
30. K.J. Choi, H.W. Jang, One-dimensional oxide nanostructures as gas-sensing materials: review and issues. *Sensors* **10**(4), 4083–4099 (2010)
31. N. Salah et al., Nanocomposites of CuO/SWCNT: promising thermoelectric materials for mid-temperature thermoelectric generators. *J. Eur. Ceram. Soc.* **39**(11), 3307–3314 (2019)
32. G.A. Slack, New materials and performance limits for thermoelectric cooling, in *CRC handbook of thermoelectrics*. (CRC Press, 2018), pp.407–440
33. H. Li et al., High performance $\text{In}_x\text{Ce}_y\text{Co}_4\text{Sb}_{12}$ thermoelectric materials with in situ forming nanostructured InSb phase. *Appl. Phys. Lett.* **94**, 102114–102114 (2009)
34. W. Xie et al., Simultaneously optimizing the independent thermoelectric properties in (Ti, Zr, Hf)(Co, Ni) Sb alloy by in situ forming InSb nanoinclusions. *Acta Mater.* **58**(14), 4705–4713 (2010)
35. W. Liu et al., Recent advances in thermoelectric nanocomposites. *Nano Energy* **1**(1), 42–56 (2012)
36. J. Zide et al., High efficiency semimetal/semiconductor nanocomposite thermoelectric materials. *J. Appl. Phys.* **108**(12), 123702 (2010)
37. L. Chen, Y.-B. Chen, L.-M. Wu, Synthesis of uniform Cu₂S nanowires from Copper–thiolate polymer precursors by a solventless thermolytic method. *J. Am. Chem. Soc.* **126**(50), 16334–16335 (2004)
38. T. Ohtani et al., Synthesis of binary copper chalcogenides by mechanical alloying. *Mater. Res. Bull.* **30**(12), 1495–1504 (1995)
39. Y. Wang et al., One-pot synthesis and optical property of copper (I) sulfide nanodisks. *Inorg. Chem.* **49**(14), 6601–6608 (2010)
40. Y. Zhang et al., Electronic structure of antifluorite Cu₂X (X= S, Se, Te) within the modified Becke–Johnson potential plus an on-site Coulomb U. *J. Chem. Phys.* **140**(7), 074702 (2014)
41. L. Mi et al., Large-scale urchin-like micro/nano-structured NiS: controlled synthesis, cation exchange and lithium-ion battery applications. *RSC Adv.* **3**(38), 17431–17439 (2013)
42. Y. Zhang et al., Effect of ether electrolyte on the electrochemical performance of Cu₂S. *Int. J. Electrochem. Sci.* **15**, 2903–2912 (2020)
43. J.V. Lima et al., Synthesis and characterization of Cu_{2-x}S structures by different chemical routes for electronic applications. *Mater. Res.* **24**, e20210018 (2021)
44. K. Nemade, S. Waghuley, LPG sensing performance of CuO–Ag₂O bimetallic oxide nanoparticles. *St. Petersburg. Univ. J. Phys. Math.* **1**(3), 249–255 (2015)
45. H. Bao et al., Crystal-plane-controlled surface restructuring and catalytic performance of oxide nanocrystals. *Angew. Chem.* **123**(51), 12502–12506 (2011)
46. D. Chen et al., Hot-injection synthesis of Cu-doped Cu₂ZnSnSe₄ nanocrystals to reach thermoelectric zT of 0.70 at 450 C. *ACS Appl. Mater. Interfaces* **7**(44), 24403–24408 (2015)
47. K. Kumar Choudhary et al., Phonon scattering mechanism for size-dependent thermoelectric properties of Bi₂Te₃ nanoparticles. *ChemistrySelect* **7**(34), e202202503 (2022)
48. A.B. Devi et al., Novel synthesis and characterization of CuO nanomaterials: Biological applications. *Chin. Chem. Lett.* **25**(12), 1615–1619 (2014)
49. N. Tamaekong, C. Liewhiran, S. Phanichphant, Synthesis of thermally spherical CuO nanoparticles. *J. Nanomater.* **2014**, 507978 (2014)
50. U.A. Joshi, P.A. Maggard, CuNb₃O₈: a p-type semiconducting metal oxide photoelectrode. *J. Phys. Chem. Lett.* **3**(11), 1577–1581 (2012)
51. A. Pop et al., Optical properties of cuxs nano-powders. *Chalcogenide Lett.* **8**(6), 363–370 (2011)
52. X. Yu, X. An, Controllable hydrothermal synthesis of Cu₂S nanowires on the copper substrate. *Mater. Lett.* **64**(3), 252–254 (2010)
53. S. Fu et al., Enhanced photo-electrochemical activity of ZnO/Cu₂S nanotube arrays photocathodes. *Int. J. Hydrog. Energy* **46**(21), 11544–11555 (2021)
54. D. Han et al., Engineering charge transfer characteristics in hierarchical Cu₂S QDs@ ZnO nanoneedles with p–n heterojunctions: towards highly efficient and recyclable photocatalysts. *Nanomaterials* **9**(1), 16 (2018)
55. P. Zhang, L. Gao, Copper sulfide flakes and nanodisks. *J. Mater. Chem.* **13**(8), 2007–2010 (2003)
56. M. Singh, A. Singhal, Modeling of shape and size effects for the band gap of semiconductor nanoparticles, in *2018 2nd International Conference on Micro-Electronics and Telecommunication Engineering (ICMETE)*. (IEEE, 2018), pp.10–15
57. S. Ahmad et al., Electronic and optical properties of semiconductor and alkali halides. *Arab. J. Sci. Eng.* **38**(7), 1889–1894 (2013)
58. W.A.A. Alhassan, I.A. Wadi, Determination of optical energy gap for copper oxide at different temperatures. *Int. J. Adv. Eng. Res. Sci.* **5**(3), 237422 (2018)
59. T. Hong et al., Enhanced thermoelectric performance in SnTe due to the energy filtering effect introduced by Bi₂O₃. *Mater. Today Energy* **25**, 100985 (2022)
60. X. Zhang et al., Spontaneously promoted carrier mobility and strengthened phonon scattering in p-type YbZn₂Sb₂ via a nanocompositing approach. *Nano Energy* **43**, 159–167 (2018)
61. A. Putnis, The transformation behaviour of cuprous sulphides and its application to the efficiency of Cu_xS–CdS solar cells. *Philos. Mag.* **34**(6), 1083–1086 (1976)
62. P. Lukashev et al., Electronic and crystal structure of Cu_{2-x}S: full-potential electronic structure calculations. *Phys. Rev. B* **76**(19), 195202 (2007)
63. R. Venkatasubramanian, Lattice thermal conductivity reduction and phonon localizationlike behavior in superlattice structures. *Phys. Rev. B* **61**(4), 3091 (2000)
64. Z. Xiong et al., Solution-processed CdS/Cu₂S superlattice nanowire with enhanced thermoelectric property. *ACS Appl. Mater. Interfaces* **9**(38), 32424–32429 (2017)
65. G. Mahan, J. Sofo, M. Bartkowiak, Multilayer thermionic refrigerator and generator. *J. Appl. Phys.* **83**(9), 4683–4689 (1998)
66. Z. Zhang et al., Thermoelectric properties of multi-walled carbon nanotube-embedded Cu₂S thermoelectric materials. *J. Mater. Sci. Mater. Electron.* **30**(5), 5177–5184 (2019)
67. A. Pakdel et al., Enhanced thermoelectric performance of Bi–Sb–Te/Sb₂O₃ nanocomposites by energy filtering effect. *J. Mater. Chem. A* **6**(43), 21341–21349 (2018)
68. B.J. Van Zeghbroeck, *Principles of semiconductor devices* (Bart Van Zeghbroeck, 2011)
69. C. Hu et al., Carrier grain boundary scattering in thermoelectric materials. *Energy Environ. Sci.* **15**(4), 1406–1422 (2022)
70. P. Dharmiah et al., Influence of powder size on thermoelectric properties of p-type 25% Bi₂Te₃75% Sb₂Te₃ alloys fabricated using gas-atomization and spark-plasma sintering. *J. Alloys Compd.* **686**, 1–8 (2016)
71. D. Liang et al., A facile synthetic approach for copper iron sulfide nanocrystals with enhanced thermoelectric performance. *Nanoscale* **4**(20), 6265–6268 (2012)
72. K. Suekuni et al., High-performance thermoelectric minerals: colusites Cu₂₆V₂M₆S₃₂ (M=Ge, Sn). *Appl. Phys. Lett.* **105**(13), 132107 (2014)

73. Z.-H. Ge et al., Synthesis and transport property of Cu_{1.8}S as a promising thermoelectric compound. *Chem. Commun.* **47**(47), 12697–12699 (2011)
74. X. Liang, D. Jin, F. Dai, Phase transition engineering of Cu₂S to widen the temperature window of improved thermoelectric performance. *Adv. Electron. Mater.* **5**(10), 1900486 (2019)
75. R. Mulla, M. Rabinal, Ambient growth of highly oriented Cu₂S dendrites of superior thermoelectric behaviour. *Appl. Surf. Sci.* **397**, 70–76 (2017)
76. H. Tang et al., Graphene network in copper sulfide leading to enhanced thermoelectric properties and thermal stability. *Nano Energy* **49**, 267–273 (2018)

Publisher's Note Springer Nature remains neutral with regard to jurisdictional claims in published maps and institutional affiliations.

Springer Nature or its licensor (e.g. a society or other partner) holds exclusive rights to this article under a publishing agreement with the author(s) or other rightsholder(s); author self-archiving of the accepted manuscript version of this article is solely governed by the terms of such publishing agreement and applicable law.